

1  
2  
3  
4  
5  
6  
7  
8  
9  
10  
11  
12  
13  
14  
15  
16  
17  
18  
19

**Groundwater flow and salt transport in a subterranean estuary  
driven by intensified wave conditions**

**Clare Robinson<sup>a,1</sup>, Pei Xin<sup>b,c</sup>, Ling Li<sup>b,c</sup>, D. A. Barry<sup>d</sup>**

<sup>a</sup>Department of Civil Engineering, Western University, London, Canada.

Email: [crobinson@eng.uwo.ca](mailto:crobinson@eng.uwo.ca)

<sup>b</sup>National Centre for Groundwater Research and Training, School of Civil Engineering, The University of Queensland, Queensland, Australia.

Emails: [p.xin@uq.edu.au](mailto:p.xin@uq.edu.au); [l.li@uq.edu.au](mailto:l.li@uq.edu.au)

<sup>c</sup>State Key Laboratory of Hydrology-Water Resources and Hydraulic Engineering, Hohai University, Nanjing, China.

<sup>d</sup>Laboratoire de technologie écologique, Institut d'ingénierie de l'environnement, Faculté de l'environnement naturel, architectural et construit (ENAC), Station 2, Ecole Polytechnique Fédérale de Lausanne (EPFL), 1015 Lausanne, Switzerland.

Email: [andrew.barry@epfl.ch](mailto:andrew.barry@epfl.ch)

Resubmitted to *Water Resources Research* on 29 November 2013

20 **KEY POINTS**

- 21 • Intensified waves perturb flow and transport in a subterranean estuary.
- 22 • Lengthy period (months) for salinity distribution to recover from an intensified wave event.
- 23 • Exchange fluxes and flow patterns respond and recover rapidly following an intensified wave
- 24 event.

25 **ABSTRACT**

26 A numerical study, based on a density-dependent variably saturated groundwater flow model,  
27 was conducted to investigate flow and salt transport in a near-shore aquifer under intensified  
28 wave conditions caused by offshore storms. Temporally varying onshore hydraulic gradients due  
29 to wave set-up were determined as the seaward boundary condition for the simulated aquifer.  
30 The results showed a rapid increase in influxes across the aquifer-ocean interface in response to  
31 the wave event followed by a more gradual increase in effluxes. The upper saline plume first  
32 widened horizontally as the wave set-up point moved landward. It then expanded vertically with  
33 recirculating seawater pushed downwards by the wave-induced hydraulic gradient. The time for  
34 the salt distribution to return to the pre-storm condition was up to a hundred days, and correlated  
35 strongly with the time for seawater to recirculate through the aquifer. The pathways of  
36 recirculating seawater and fresh groundwater were largely modified by the wave event. These  
37 pathways crossed through the same spatial locations at similar times, indicating significant salt-  
38 freshwater mixing. The flow and salt transport dynamics were more responsive to wave events of  
39 longer duration and higher intensity, especially in more permeable aquifers with lower fresh  
40 groundwater discharge. Despite their larger response, aquifers with higher permeability and  
41 beach slope recovered more rapidly post-event. The rapid recovery of the flows compared with  
42 the salinity distribution should be considered in field data interpretation. Due to their long-lasting  
43 impact, wave events may significantly influence the geochemical conditions and the fate of  
44 chemicals in a subterranean estuary.

45 **KEYWORDS:** wave effects, submarine groundwater discharge, aquifer-ocean exchange, coastal  
46 aquifer, numerical modeling.

## 47 **1. Introduction**

48 Submarine groundwater discharge (SGD) from a coastal aquifer provides a significant transport  
49 pathway for delivering land-sourced chemicals (e.g., nutrients, pharmaceuticals, industrial  
50 pollutants) to coastal water [e.g., *Brovelli et al.*, 2007; *Burnett et al.*, 2003; *Johannes*, 1980].  
51 Chemical loading rates via SGD are strongly controlled by the subsurface flow paths and  
52 geochemical conditions in the aquifer, particularly near the shore [*Kroeger and Charette*, 2008;  
53 *Robinson et al.*, 2009; *Slomp and van Cappellen*, 2004; *Spiteri et al.*, 2008a; *Westbrook et al.*,  
54 2005]. Due to the different chemical compositions of meteoric groundwater and seawater, the  
55 mixing of these waters as seawater recirculates through the near-shore aquifer can form an  
56 important reaction zone [*Appelo*, 1994]. This zone, termed a subterranean estuary [*Moore*, 1999],  
57 is typically characterized by strong geochemical gradients (e.g., pH and redox) where land-  
58 derived chemicals may be transformed or attenuated prior to their discharge [*Charette et al.*,  
59 2005; *Hays and Ullman*, 2007; *Loveless and Oldham*, 2010; *Spiteri et al.*, 2005]. This zone also  
60 plays an important role in the transformation of sea-derived constituents recirculating through the  
61 near-shore aquifer [*Anschutz et al.*, 2009; *Spiteri et al.*, 2008b].

62 Driven by density gradients, seawater intrudes the aquifer forming a saltwater wedge [*Diersch*  
63 *and Kolditz*, 2002; *Smith*, 2004; *Voss and Souza*, 1987; *Werner et al.*, 2013]. In the absence of  
64 sea level oscillations, the dispersion (mixing) zone along the saltwater wedge interface is the  
65 primary area of salt-freshwater mixing in a near-shore aquifer [*Moore*, 1999]. However, sea level  
66 oscillations occur at natural coasts due to tides and waves. Tides acting on a sloping beach face  
67 drive water exchange across the aquifer-ocean interface with infiltration dominating in the upper  
68 intertidal region and exfiltration dominating near the low-tide mark. This results in the formation  
69 of an upper saline plume (USP) in addition to the saltwater wedge [*Boufadel*, 2000; *Mango et al.*,

70 2004; *Robinson et al.*, 2007b]. In the presence of waves, an USP also forms primarily because  
71 waves induce an onshore upward tilt in the phase-averaged sea level (wave set-up; Figure 1a).  
72 This pressure gradient sets up a seawater recirculation cell through the near-shore aquifer that  
73 extends from the maximum wave run-up to wave-breaking point [*Bakhtyar et al.*, 2012;  
74 *Bakhtyar et al.*, 2013; *Li and Barry*, 2000; *Longuet-Higgins*, 1983; *Xin et al.*, 2010]. Recently,  
75 *Xin et al.* [2010] simulated the combined effects of both tides (semi-diurnal) and constant swell  
76 waves acting on a sloping beach and showed that when these forces are combined a more  
77 extensive USP is created with increased seawater recirculation across the aquifer-ocean interface.  
78 When an USP forms, the fresh groundwater discharge location is pushed seaward and is confined  
79 between the saltwater wedge and the USP (Figure 1a) [*Boufadel*, 2000; *Robinson et al.*, 2007b;  
80 *Xin et al.*, 2010]. Characterized by significantly faster seawater recirculation rates and shorter  
81 transit times than the saltwater wedge [*Robinson et al.*, 2007b], the USP represents an active  
82 zone of salt-freshwater mixing in a near-shore aquifer.

83 For regular oceanic forcing conditions (semi-diurnal tides, constant swell waves), the salt-  
84 freshwater mixing in a subterranean estuary is driven primarily by hydrodynamic dispersion  
85 enhanced by flow oscillations and to a limited extent density instabilities (for USP). *Robinson et*  
86 *al.* [2007a] and *Abarca et al.* [2013] presented field and numerical results that demonstrated  
87 strong influences of spring-neap tidal variations on pore-water flow and solute (salt) transport in  
88 the near-shore aquifer. *Robinson et al.* [2007a] showed that the tidal variations caused significant  
89 changes in the salinity distribution with the USP contracting and expanding between the spring  
90 and neap tides (period = 14.78 d). At the field site of *Abarca et al.* [2013], due to the different  
91 magnitude of the new moon and full moon spring tides, the USP expanded and contracted at a  
92 period of four weeks. The extent of variation in the USP size observed by *Abarca et al.* [2013]

93 was greater than reported by *Robinson et al.* [2007a]. For both studies, the oscillation of the USP  
94 driven by the longer period spring-neap tidal variations caused significantly greater salt-  
95 freshwater mixing than induced by the semi-diurnal tidal fluctuations. Varying wave conditions  
96 may also modify significantly the near-shore aquifer dynamics, causing large displacement of the  
97 USP, especially for longer-duration events with large wave height variations. Therefore wave  
98 events may have a significant impact on the salt-freshwater mixing and the geochemical  
99 conditions in a subterranean estuary.

100 A number of investigations have examined coastal aquifer salinization caused by episodic (very  
101 large) storm events where the beach is overtopped and the coastal plain is inundated by seawater.  
102 These storm events can have a significant and long-lasting (order of months) influence on the  
103 salinity distribution and flows in the coastal aquifer. Effects of storms on the coastal aquifer  
104 system however are not limited to extreme events. Changes in subsurface flow patterns and  
105 salinity distributions are also induced by small offshore storms that generate intensified wave  
106 conditions along a shoreline. *Cartwright et al.* [2004] conducted a field study on a sandy beach  
107 aquifer and showed considerable oscillations of the saltwater wedge (3-5 m) in response to a  
108 wave event during which the significant wave height increased from 0.4 to 4.5 m over a period  
109 of  $\sim 2$  d. *Li et al.* [2004] developed an analytical expression to describe watertable fluctuations  
110 induced by intensified wave conditions. While studies have revealed the influence of intensified  
111 wave conditions on the near-shore aquifer, the effect on the groundwater flows, solute transport,  
112 salt-freshwater mixing and water exchange rates remain poorly quantified. Also, the time scales  
113 for the response to and recovery of the system from wave events are not clear. With smaller  
114 offshore storms occurring frequently and generating intensified wave conditions along coastlines

115 [Nielson, 2009], this knowledge is needed to better understand salt-freshwater mixing dynamics  
116 and geochemical conditions in a nearshore aquifer.

117 In this study, numerical simulations were conducted to examine the impact of intensified wave  
118 conditions induced by an offshore storm on groundwater flow and salt transport in a near-shore  
119 aquifer. Simulated events with increased wave height (up to  $H_{rms} = 7$  m) were considered – these  
120 provided the seaward boundary condition specified via time-varying wave-induced onshore  
121 hydraulic gradients (wave set-up). Tidal fluctuations were not simulated, and as such the findings  
122 are pertinent for micro-tidal beaches that are dominated by wave rather than tidal effects  
123 [Masselink and Short, 1993]. Wave events will also impact the groundwater flows and salt  
124 transport in tidally-influenced beaches, and the combined effects of tides and waves will lead to  
125 more complex conditions as suggested by Xin et al. [2010]. Large episodic events (e.g.  
126 hurricanes, tsunami) that result in beach overtopping and seawater inundation of the coastal plain  
127 are also beyond the scope of this study. The aim was to quantify the influence of a wave event on  
128 the water and salt exchange across the aquifer-ocean interface, near-shore groundwater flows and  
129 salinity distribution in the aquifer. Key controlling variables including the intensity and duration  
130 of the wave event, the magnitude of fresh groundwater discharge, hydraulic conductivity and  
131 beach slope were examined.

## 132 **2. Numerical model**

133 A numerical model based on SUTRA [Voss and Provost, 2002] was developed to simulate  
134 variably saturated, density-dependent pore-water flow and salt transport in an unconfined coastal  
135 aquifer subject to time-varying wave forcing conditions (Figure 1). This model is similar to that  
136 used and described by Xin et al. [2010].

137 The model domain represented a 2-D cross-shore transect through a homogeneous and isotropic  
 138 coastal aquifer with a thickness of 33 m and a sloping beach boundary (beach slope = 0.1)  
 139 (Figure 1b). It was assumed that groundwater flow and solute transport were negligible in the  
 140 alongshore direction. The  $x$ - $z$  co-ordinate origin was located at the shoreline location  
 141 corresponding to the still sea water level (SWL). With the exception of the wave forcing  
 142 conditions, the parameters and boundary conditions adopted for the base case (Case 1) were the  
 143 same as for the base case of *Xin et al.* [2010]. The parameter values were representative of a  
 144 typical sandy coastal aquifer system [*Robinson et al.*, 2006] with hydraulic conductivity  $K_s = 10$   
 145  $\text{md}^{-1}$ , porosity  $\phi = 0.45$ , longitudinal dispersivity  $\alpha_L = 0.5$  m and transverse dispersivity  $\alpha_T =$   
 146  $0.05$  m. For the *van Genuchten* [1980] formulas,  $S_{wres} = 0.1$  while the parameters  $n$  and  $\alpha$  were  
 147 set to  $14.5 \text{ m}^{-1}$  and  $2.68$ , respectively [*Carsel and Parrish*, 1988].

148 *Xin et al.* [2010] recently demonstrated that a wave set-up approach can be adopted to simulate  
 149 the effects of waves acting on the seaward boundary rather than simulating instantaneous waves.  
 150 This approach is significantly more efficient and retains the key effects of waves on the  
 151 groundwater flow and solute transport processes as well as the exchange of water and solutes  
 152 across the aquifer-ocean interface. Using an empirical formula of *Nielson* [2009], we determined  
 153 the mean sea surface elevation (averaged over a wave period),  $\eta$  (m):

$$\eta = \frac{0.4H_{rms}}{1 + 10 \frac{D + \eta}{H_{rms}}} \quad (1)$$

154 where  $H_{rms}$  (m) is the root mean square wave height at time  $t$ , and  $D$  (m) is the still water depth at  
 155 location  $x$  (Figure 1a). This expression was solved for  $\eta$ , which thereby defined the hydraulic  
 156 head condition on the seaward boundary of the groundwater model. Other solutions describing

157 wave set-up are available, including that by *Longuet-Higgins* [1983], or alternatively, as done by  
 158 *Xin et al.* [2010], the instantaneous wave motion predicted by a shallow water wave simulator  
 159 such as BEACHWIN [*Li et al.*, 2002] may be used to derive the mean sea surface elevation with  
 160 the wave set-up effect included. Equation (1) does not consider wave run-up (in the swash zone  
 161 further inland) and may thus predict a smaller wave set-up compared with those of *Longuet-*  
 162 *Higgins* [1983] and *Li et al.* [2002]. As this study focused on providing mechanistic insights into  
 163 the effects of an intensified wave event on near-shore aquifer dynamics and the time-scale of the  
 164 system's response, the numerical findings are expected to be consistent regardless of the specific  
 165 solution adopted to simulate wave set-up.

166 Synthetic time series of  $H_{rms}$  were generated to represent a wave event of a given duration and  
 167 intensity (Figure 2) using:

$$H_{rms}(t) = H_{rms}^{SS} + H_{rms}^{INC} \exp \left[ - \left( \frac{t - T_{max}}{F} \right)^2 \right], \quad (2)$$

168 where  $T_{max}$  [T] is the time at which the maximum wave height occurs (day 6 for all simulations);  
 169  $F$  [T] is a parameter that controls the duration of the wave event (period of the wave event is  
 170 equal to approximately  $5F$ );  $H_{rms}^{SS}$  is the steady state wave height (pre- and post-wave event); and  
 171  $H_{rms}^{INC}$  is the maximum increase in wave height. Synthetic wave events were simulated so that the  
 172 response and recovery of the near-shore aquifer could be readily quantified. Note that equation  
 173 (2) has been found to describe well the wave height variations over real offshore storm events  
 174 [*Cartwright et al.*, 2004].

175 For all simulations performed,  $H_{rms}^{SS}$  was set to 1 m. Cases were simulated with  $F$  varying from  
 176 0.5 to 2 d and  $H_{rms}^{INC}$  varying from 2 to 6 m (Table 1). Along a typical wave-exposed coastline, the

177 smaller wave events simulated (i.e.,  $H_{rms}^{INC} = 2$ ) would occur relatively often (order of months),  
178 whereas the large wave events simulated would be infrequent (order of decades). To put into  
179 context, historical data for the New South Wales (Australia) coastline with a moderate wave  
180 climate shows that the maximum wave heights ( $H_{rms}$ ) for return periods of 0.1, 1, 10 and 50 years  
181 are 2.5, 3.8, 4.9 and 5.7 m, respectively [Shand *et al.*, 2010].

182 Additional simulations were conducted to examine the extent to which land-derived groundwater  
183 flux, the aquifer permeability and the beach slope altered the system's response to the intensified  
184 wave conditions (Table 1). Aquifer hydraulic conductivities ranging from  $K = 6.66 - 50 \text{ md}^{-1}$   
185 were considered. This range represents the permeability of medium sand which is common on  
186 wave dominated beaches. Although,  $K$  can vary over several orders of magnitude in nearshore  
187 aquifers, the  $K$  range considered was constrained by the model domain adopted. For example,  
188 higher  $K$  values reduced the landward hydraulic gradient and subsequently the intrusion of the  
189 saltwater wedge became restricted by the landward model boundary. Beach slopes from steep ( $\beta$   
190 = 0.1) to moderately steep ( $\beta = 0.05$ ) were examined. The range of  $\beta$  considered was restricted  
191 by the wave set-up formula used (Equation 1) which is not applicable for more mildly sloping  
192 beaches ( $\beta < 0.05$ ).

193 The boundary condition applied on the aquifer-ocean interface (**BCD**) depended on the sea  
194 surface elevation ( $\eta$ ), which varied with the wave height (Figure 1). The submerged nodes along  
195 the interface (below the sea surface) were prescribed by the hydrostatic pressure corresponding  
196 to the local mean water depth described by (1). Above the sea surface the exposed nodes were  
197 either (a) considered seepage face nodes with local pressure equal to the atmospheric pressure ( $P$   
198 = 0) if the nodes were saturated at the previous time step, or (b) treated as part of the no-flow

199 boundary above the seepage face if the nodes were unsaturated at the previous time step. The  
200 maximum wave set-up point never exceeded the apex of the sloped beach face (**B**). Influx to the  
201 aquifer across the interface had a salt concentration of 35 ppt (mass fraction) and at nodes with  
202 efflux (from the aquifer) a zero concentration gradient was specified. The vertical seaward  
203 boundary condition (**DE**) was no flow. The location of this boundary was set sufficiently far  
204 from the shoreline (at  $x = 50$  m) so as not to influence the near-shore subsurface flow and  
205 transport.

206 A uniform, constant flux ( $Q_f$ ) was specified along the vertical landward boundary (**AF**) to  
207 simulate fresh groundwater flow towards the sea. For all simulations except Cases 7-9, the flow  
208 rate through the landward boundary was specified as  $2.1 \text{ m}^3\text{d}^{-1}$  per meter width of aquifer with a  
209 background salt concentration of 1 ppt. This  $Q_f$  corresponds with the estimated freshwater flux at  
210 a field site on the Moreton Island, Australia [Robinson *et al.*, 2006]. The bottom model boundary  
211 (**EF**) was an impermeable aquifer base and thus set as a no-flow boundary. The upper boundary  
212 (**AB**) was also a no-flow boundary with rainfall and evaporation neglected.

213 The model was initially run to steady state with the pre-storm wave condition (with  $H_{rms}^{SS} = 1$  m)  
214 applied at the seaward boundary. The model was then run with a time-varying seaward boundary  
215 condition to simulate the wave events shown in Figure 2. Each time-varying simulation was run  
216 for a total simulation time of 160 d. This time was required for the aquifer to return to pre-storm  
217 conditions. The initial steady state model was the same for Cases 1-6, but different for the  
218 remaining cases due to the changes in  $Q_f$ ,  $\beta$  and  $K$ . The initial steady state flows and salt  
219 concentrations for Cases 1-6 can be seen in Figure 3a. Further details of the model including the  
220 model set-up and grid discretization are given by Xin *et al.* [2010].

## 221 3. Results and Discussion

### 222 3.1 Effect of intensified wave conditions (Case 1)

223 The simulated pore-water salinity distribution and flow velocity vectors in the near-shore aquifer  
224 before, during and after the wave event for Case 1 are shown in Figure 3. As expected, the  
225 groundwater flows and salinity distribution in the aquifer were significantly modified by the  
226 intensified wave conditions. At the initial steady state, the onshore pressure gradient  
227 corresponding to  $H_{rms} = 1$  m led to a seawater recirculation cell through the shallow aquifer. This  
228 formed an USP that extended up to the wave set-up point ( $x \approx -5$  m, Figure 3a). As previously  
229 shown by *Xin et al.* [2010], the wave-induced recirculations pushed fresh groundwater to  
230 discharge below the USP. The flow pattern and salinity distribution were similar to those also  
231 observed in aquifers subjected to simple harmonic tidal fluctuations (e.g., semi-diurnal)  
232 [*Boufadel, 2000; Mango et al., 2004; Mao et al., 2006; Robinson et al., 2006; Robinson et al.,*  
233 *2007b; Xin et al., 2010*].

234 The recirculating flow strengthened and the USP expanded as the wave height increased (Figure  
235 3b). The USP initially expanded horizontally as seawater moved landward and infiltrated the  
236 foreshore area in response to the increased wave set-up. The USP reached its maximum  
237 horizontal extent at the peak of the wave event (Figure 3c) – at this time the wave set-up point  
238 was at its most landward position. As the wave height decreased, the USP gradually contracted  
239 horizontally, but with seawater continuing to infiltrate on the upper part of the beach, the USP  
240 expanded in the vertical direction (Figure 3d). Once infiltrated, seawater moved downward along  
241 a discharge flow path to the sea (Figure 3e,f). The observed extent of expansion and contraction  
242 of the USP over the wave event is similar to that observed by *Abarca et al.* [2013] in response to  
243 spring-neap tidal variations. However, unlike the cyclic variations induced by spring-neap

244 variations, wave-induced changes to the USP are driven by an irregular forcing and in some  
245 cases there may be a lengthy time gap between successive wave events. For the conditions  
246 simulated there was a significant time delay before the salinity distribution in the near-shore  
247 aquifer returned to pre-storm conditions (Figure 3g,h). Further, it is evident that residual salt was  
248 trapped in the unsaturated zone beneath the beach face as the wave event passed (Figure 3 d-h).  
249 This was due to the rapid fall of the watertable as the wave height decreased, leaving the salt  
250 behind in an unsaturated zone with relatively weak flow and solute transport. A similar salt  
251 trapping effect was observed by *Lenkopane et al.* [2009] in numerical simulations of a riparian  
252 zone exposed to tidal and seasonal estuarine salinity and water level fluctuations. In reality the  
253 trapped salt may be flushed through the shallow beach sediments by rainfall. This was not  
254 considered in the simulations. Spatial moments of salt concentrations were calculated to quantify  
255 the response of the salinity distribution to the wave event (see Auxiliary Material for calculation  
256 details). Spatial moments were calculated separately for the USP and saltwater wedge to analyze  
257 their individual behavior. This was done by dividing the model domain into two separate  
258 integration domains (upper and lower) by locating the minimum concentrations separating these  
259 two saline plumes. The background salt concentration (1 ppt) was subtracted from the salt  
260 concentrations before the moments were calculated so that only salt originating from the  
261 seawater was considered in the calculation. From Figure 4a it can be seen that the salt mass in  
262 the USP increased rapidly in response to the increase in wave height. The maximum salt mass in  
263 the aquifer occurred 1.5 d after the peak of the wave event (at 7.5 d) with salt continuing to  
264 infiltrate the foreshore more rapidly than it could exfiltrate further offshore. As the waves  
265 receded the salt mass decreased gradually with the USP slowly returning to the pre-storm  
266 condition. The salt mass in the USP returned to within 10%, 5% and 1% (surplus) of its initial

267 (pre-storm) mass at 62 d, 79 d and 106 d, respectively. Consistent with the evolution of salt  
268 distribution shown in Figure 3, the centroid of the plume moved rapidly landwards and upwards  
269 in response to the intensified waves as seawater infiltrated further landward (Figure 4b,c). After  
270 the storm peak, the centroid of the plume moved downward and gradually seaward.

271 Particle tracking was performed to examine the advective flow paths and corresponding transit  
272 times for seawater recirculating and fresh groundwater discharging through the aquifer. Particle  
273 tracking was conducted in MATLAB using the element centroid velocities output by SUTRA.  
274 Particles were released along a vertical line at  $x = -20$  m with 1 m vertical interval (called  
275 freshwater particles) and along the aquifer-ocean interface at 0.5 m interval (called saltwater  
276 particles). The particle tracking started at the beginning of the simulation. The particle flow paths  
277 including transit times for Case 1 are shown in Figure 5a. For comparison, the particle tracking  
278 results for steady state conditions ( $H_{rms} = 1$  m) are also provided (Figure 5b). The intensified  
279 wave conditions significantly altered the transport pathways of the saltwater particles. The  
280 particles that infiltrated near the maximum wave set-up point ( $x = -17$  to  $-15$  m) had a shallower  
281 pathway than those that infiltrated seaward of this point ( $x = -14$  m to  $-12$  m). This is because the  
282 latter particles were exposed to downward flow induced by the wave set-up for a longer period of  
283 time than the former particles, which were subjected to this condition only at the peak of the  
284 storm. During the wave event the saltwater particles moved downwards and crossed into the pre-  
285 storm flow paths of freshwater particles. As the wave event passed the saltwater particles then  
286 discharged along the freshwater path lines. Note that the overlap between the saltwater and  
287 freshwater particles occurs only spatially with the particles not crossing the same locations at  
288 identical times. The successive spatial overlap between the paths of saltwater and freshwater

289 particles is consistent with aquifer salinization and freshening as the USP expanded and  
290 contracted.

291 The transit times for the saltwater particles to travel through the aquifer as a function of their  
292 starting  $x$  co-ordinate along the aquifer-ocean interface are shown in Figure 6. For Case 1 the  
293 transit times were longest for particles infiltrating just seaward of the maximum wave set-up  
294 point, between  $x = -14$  and  $-12$  m. This was consistent with the longer and deeper flow paths of  
295 these particles (Figure 5a). The transit times were slightly less for particles infiltrating close to  
296 the maximum wave set-up point (between  $x = -14$  to  $-16$ ) due to their shallower and shorter flow  
297 paths. The transit times decreased almost linearly seaward of  $x = -12$  m as the flow path lengths  
298 decreased towards the center of the flow recirculation cell. The time for the total salt mass in the  
299 upper aquifer domain (USP) to recover to within 10%, 5% and 1% (surplus) of the pre-storm salt  
300 mass is presented in Figure 6b (red horizontal lines). The maximum saltwater particle transit  
301 times appear to be strongly related to the 10% (surplus) recovery time indicating that the long  
302 recovery of the salinity distribution in the upper aquifer was largely controlled by the advective  
303 transport of the infiltrated seawater. This result also demonstrates the importance of dispersive  
304 transport with approximately 10% of the excess salt remaining in the aquifer longer than the  
305 maximum advective transit time for saltwater particles (64 d). The importance of dispersive  
306 transport is reflected in the long 5% (79 d) and 1% (106 d) (surplus) recovery times; the  
307 associated salt-freshwater mixing is expected to lead to modifications in the geochemical  
308 conditions in a subterranean estuary.

309 The wave event had much less impact on the fresh groundwater discharge flow paths. The transit  
310 times for the freshwater particles (released at  $x = -20$  m) increased with aquifer depth due to the  
311 longer discharge flow path ( $\sim 150$  d and  $\sim 80$  d for particles released at  $z = -29$  m and  $z = 0$  m,

312 respectively; Figure 5). Other than the intensified wave conditions inducing a small localized  
313 circulation for freshwater particles in the upper aquifer, the event did not significantly alter the  
314 fresh groundwater pathways or transit times.

315 The calculated variances of salt in the USP (Figure 7a,b) were consistent with salinity  
316 distributions (Figure 3) and the saltwater particle tracking results (Figure 5). The equations used  
317 to calculate the variance are provided in the Auxiliary Material. Both the horizontal and vertical  
318 variance increased sharply in response to the wave event. The horizontal spread was greatest at  
319 the peak of the wave event (6 d), consistent with the rapid seawater infiltration into the upper  
320 freshwater zone. The locations of freshwater and saltwater particles at 6 d are shown in Figure  
321 7c. The similar locations for particles near the maximum wave set-up point indicate that  
322 enhanced salt-freshwater mixing occurred at this location around the peak of the wave event (6  
323 d). It should be noted that although the saltwater and freshwater particle locations are not exactly  
324 the same at a given time, hydrodynamic dispersion would cause mixing due to the close  
325 proximity of the particles. As the wave height decreased, the horizontal variance decreased as the  
326 USP contracted horizontally. In contrast, the vertical variance of the USP continued to increase  
327 for some time after the peak of the wave event. This is consistent with the downward movement  
328 of the saltwater that infiltrated just seaward of the maximum wave set-up point into the  
329 freshwater zone. The maximum vertical variance occurred at ~40 d. As seen in Figure 7d the  
330 large variance was associated with the enhanced fresh-saltwater mixing (similar locations for  
331 freshwater and saltwater particles) along the lower boundary of the USP. The variances slowly  
332 decreased to their pre-storm values as the excess salt discharged from the aquifer.

333 Although movement of the saltwater wedge interface was not clearly evident from the salt  
334 distributions (Figure 3), spatial moments reveal that the intensified wave conditions caused the

335 total salt mass in the lower aquifer to decrease (Figure 8a). There was an abrupt decline in the  
336 salt mass in response to the storm event followed by a more gradual decrease in mass. This was  
337 likely due to the storm-induced horizontal and subsequent vertical expansion of the USP. As  
338 demonstrated by *Kuan et al.* [2012], the expansion of the upper seawater recirculation cell and  
339 thus the USP causes the saltwater wedge to retreat seaward. Consistent with the reduction in salt  
340 mass, the centroid ( $x, z$ ) of the saltwater wedge shifted slightly seaward (Figure 8b,c). This shift  
341 was relatively small (by  $\sim 0.15$  m horizontally) due to the large salt mass associated with the  
342 saltwater wedge.

343 In contrast to the salt distribution, the groundwater flows responded and recovered much faster to  
344 the changing wave conditions. This is evident from the total water exchange rates (influx and  
345 efflux) across the aquifer-ocean interface through the simulation period (Figure 9). For Case 1, it  
346 can be seen that (sea) water influx increased as the onshore pressure gradient strengthened. The  
347 maximum influx occurred 0.5 d before the storm peak with the highest influx rate occurring near  
348 the wave set-up point at this time (Figure 9a). The influx was greatest at this time as the rate of  
349 change in the wave height, and therefore onshore movement of the wave-set up point, was high  
350 combined with the strengthened offshore pressure gradient driving increased recirculation. The  
351 efflux was delayed slightly (maximum  $\sim 1$  d after the peak) and mildly more spread out relative  
352 to the influx (Figure 9b). The difference between the influx and efflux reflects the fact that the  
353 aquifer could fill more quickly than it could drain. The water exchange rates returned to within  
354 1% of the pre-storm rates within  $\sim 10$  d after the storm peak, i.e., at  $\sim 16$  d; this time lag was small  
355 compared with the response of the salt distribution. The maximum efflux ( $5.8 \text{ m}^3 \text{d}^{-1} \text{m}^{-1}$ ) was  
356 significantly greater than that predicted to be induced by regular wave forcing ( $3.3 \text{ m}^3 \text{d}^{-1} \text{m}^{-1}$  for  
357  $H_{rms} = 1$  m [steady state condition]) or semi-diurnal tidal fluctuations ( $2.8 \text{ m}^3 \text{d}^{-1} \text{m}^{-1}$  for tidal

358 amplitude = 1 m [Robinson et al., 2007b]) for the same aquifer conditions. It was also greater  
359 than that simulated by Abarca et al [2013] to be induced by spring-neap tidal variations. For  
360 their case, a maximum discharge of  $\sim 1.3 \text{ m}^3 \text{ d}^{-1} \text{ m}^{-1}$  occurred around the highest spring tides.

361 The response of the salt fluxes to the wave event was similar to that of the water fluxes (Figure  
362 9c,d). The net salt flux was positive around the peak of the wave event corresponding to the  
363 increasing salt mass in the USP (Figure 4a). The maximum salt mass in the USP occurred at 7.5  
364 d, which corresponds to the net salt flux (influx – efflux) becoming negative. For a long time  
365 after the storm (e.g., at 40 d), the net salt flux remained slightly negative. This is because  
366 (excess) salt continued to discharge from the aquifer until the salt distribution returned to the pre-  
367 storm condition.

### 368 **3.2 Effect of magnitude of wave height variation**

369 To examine the effect of the magnitude of the wave event on the near-shore aquifer dynamics  
370 simulations were conducted with  $H_{rms}^{INC}$  varying from 2-6 m (Cases 2-4, Figure 2). As expected  
371 the larger wave events increased the water and salt fluxes across the aquifer-ocean interface  
372 (Figure 9) and further modified the salinity distribution and groundwater flows. As shown in  
373 Figure 10 for Case 2 ( $H_{rms}^{INC} = 5 \text{ m}$ ), as the maximum wave set-up point moved further onshore  
374 with increased  $H_{rms}^{INC}$ , seawater infiltrated further landward and the initial horizontal and  
375 subsequent vertical expansion of the USP increased accordingly. Also, as the fall of the  
376 watertable was more rapid with increased  $H_{rms}^{INC}$ , more residual salt was trapped in the unsaturated  
377 zone beneath the beach face as the wave event passed (Figure 10).

378 The water and salt influx and efflux across the aquifer-ocean interface showed the same temporal  
379 response to the wave event for Cases 1-4, but the rates rose as the intensity of the wave event

380 increased (Figure 9). For example, relative to Case 1 ( $7.6 \text{ m}^3 \text{d}^{-1} \text{m}^{-1}$ ;  $H_{rms}^{INC} = 3 \text{ m}$ ), the maximum  
381 instantaneous influx rose by 76% for Case 2 ( $13.3 \text{ m}^3 \text{d}^{-1} \text{m}^{-1}$ ;  $H_{rms}^{INC} = 5 \text{ m}$ ), 128% for Case 3 ( $17.3$   
382  $\text{m}^3 \text{d}^{-1} \text{m}^{-1}$ ;  $H_{rms}^{INC} = 6 \text{ m}$ ) and decreased by 25% for Case 4 ( $5.8 \text{ m}^3 \text{d}^{-1} \text{m}^{-1}$ ;  $H_{rms}^{INC} = 2 \text{ m}$ ). The total  
383 storm-driven influx was calculated for each case by integrating the increase in influx (influx  
384 above the steady state influx rate) over the simulation period. As expected the total storm-driven  
385 influx also increased with the intensity of the wave event ( $53.8 \text{ m}^3 \text{m}^{-1}$  for Case 3 c.f.  $20.2 \text{ m}^3 \text{m}^{-1}$   
386 for Case 1; Table 1). For all cases, the time of the maximum influx occurred 0.5 d prior to the  
387 peak of the wave event and both the water and salt exchange rates returned rapidly to the pre-  
388 storm conditions.

389 Consistent with the salt distributions (Figures 3 and 10) and seawater influx rates, the increase in  
390 salt mass in the USP was greater for more intense wave events (Figure 4a, Table 1); so were the  
391 horizontal and vertical movement of the plume (Figure 4b,c) and the plume variance (Figure  
392 7a,b). The temporal response of the spatial moments to the wave event was similar, i.e., a sharp  
393 increase in salt mass as the waves intensified followed by a period of relatively constant mass  
394 before the mass slowly decreased to the pre-storm condition. Due to the larger disturbance, the  
395 time for the USP salt mass to return to the pre-storm condition was greater for larger wave events  
396 (Case 3 - 115 d, Case 2 - 99 d, Case 1 - 62 d and Case 4 - 49 d for the salt mass to return to  
397 within 10% of pre-storm condition). It is evident from particle tracking results shown in Figure  
398 6a that the longer recovery time of the salt distribution for the simulations with larger  $H_{rms}^{INC}$  was  
399 largely due to and corresponded with the longer advective transit times of saltwater particles  
400 infiltrating just seaward of the maximum wave set-up point. The saltwater particles infiltrating  
401 this zone were pushed deeper into the aquifer by the greater onshore pressure gradient and so  
402 their flow pathway was lengthened. For Cases 2 and 3 the salt mass in the aquifer had not

403 returned to pre-storm conditions at the end of the simulation time, indicating the enhanced  
404 dispersion in the upper aquifer. The temporal variability in the spatial moments calculated for the  
405 saltwater wedge was similar for all cases with varying  $H_{rms}^{INC}$  but intensified wave conditions  
406 pushed the saltwater wedge further seaward near the freshwater discharge zone due the larger  
407 expansion of the USP. This is evident in Figure 10 and supported by the decrease in salt mass  
408 and  $z_c$  and increase in  $x_c$  for the saltwater wedge for Cases 2 and 3 (Figure 8).

### 409 **3.3 Effect of duration of wave event**

410 Case 5 ( $F = 1$  d) and Case 6 ( $F = 0.5$  d) were conducted to evaluate the effect of the duration of  
411 the wave event on the aquifer response. The water influx and efflux rates, and the spatial  
412 moments of the USP are shown in Figures 11 and 12, respectively. For a longer duration wave  
413 event, more time was available for seawater to infiltrate the foreshore landward of the steady  
414 state wave set-up point. For all cases (Cases 1, 5 and 6) the period of increased water influx  
415 corresponded closely with the duration of the wave event with negligible time delay (Figure  
416 11a). The shorter duration events led to a higher instantaneous water influx; however the total  
417 water influx over the wave event increased as the duration of the event lengthened (Table 1).

418 The greater total water influx led to a larger USP as indicated by the total salt mass in the upper  
419 aquifer domain (Figure 12a, Table 1). The temporal trends in the spatial moments were similar  
420 among Cases 1, 5 and 6 but with different magnitudes. The duration of the storm had a greater  
421 effect on the relative vertical expansion (Figure 12c,e) of the USP than the horizontal expansion  
422 (Figure 12b,d). This is because for all cases the maximum wave height and thus the excursion of  
423 the wave set-up point was the same. For the longer duration event, saltwater particles infiltrating  
424 near the maximum wave set-up point were exposed to the onshore pressure gradient for a longer

425 time period and so these particles were pushed deeper into the aquifer. This led to the formation  
426 of a deeper USP.

427 The time for the salt distribution in the upper aquifer to recover to within 10% (surplus) of the  
428 pre-storm conditions was similar among the three cases: 62 d for Case 1, 61 d for Case 5 and 60  
429 d for Case 5 (Table 1). These recovery times increased slightly as the duration of the wave event  
430 increased and for all cases corresponded well with the maximum advective transit times of  
431 saltwater particles (Figure 6b). Due to the deeper wave-induced seawater recirculation and  
432 expanded USP, the interface of the saltwater wedge near the freshwater discharge zone was  
433 pushed slightly further seaward as the duration of the wave event increased. This was evident  
434 from the spatial moments calculated for the lower domain where the decrease in total salt mass  
435 and shift in  $x_c$  was greater for the longer wave event. For example, for Case 1 ( $F = 2$  d) the total  
436 salt mass in the lower aquifer domain decreased by  $235 \text{ kgm}^{-1}$  and  $x_c$  moved by 0.25 m in the  
437 seawater direction compared with a  $42 \text{ kgm}^{-1}$  salt mass decrease and 0.04 m seaward shift in  $x_c$   
438 for Case 6 ( $F = 0.5$  d).

### 439 **3.4 Effect of freshwater discharge rate**

440 The inland forcing provided by the fresh groundwater flux ( $Q_f$ ) dampened the impact of the wave  
441 event on the near-shore salt transport but, for the conditions simulated, it did not significantly  
442 affect the storm-induced water and salt fluxes across the aquifer-ocean interface. The water  
443 influx and efflux across the aquifer-ocean interface for Case 1 ( $Q_f = 2.1 \text{ m}^3 \text{d}^{-1} \text{m}^{-1}$ ), Case 7 ( $Q_f =$   
444  $3.15 \text{ m}^3 \text{d}^{-1} \text{m}^{-1}$ ), Case 8 ( $Q_f = 1.4 \text{ m}^3 \text{d}^{-1} \text{m}^{-1}$ ) and Case 9 ( $Q_f = 1 \text{ m}^3 \text{d}^{-1} \text{m}^{-1}$ ) are shown in Figure 13.  
445 For the initial conditions, the net flux was equal to  $Q_f$  and so the water efflux and net flux were  
446 less for the cases with reduced  $Q_f$  (Cases 8 and 9). The initial influxes were slightly higher for  
447 Cases 8 and 9 because the reduced freshwater discharge restricted less the wave- and density-

448 induced seawater recirculation. For the conditions simulated, the influx rates responded similarly  
449 to the event; the total storm-induced water influx was only slightly greater for the cases with  
450 lower fresh groundwater discharge ( $18.1 \text{ m}^3 \text{ d}^{-1} \text{ m}^{-1}$  for Case 7 c.f.  $23.2 \text{ m}^3 \text{ d}^{-1} \text{ m}^{-1}$  for Case 9; Table  
451 1).

452 The fresh groundwater discharge had a greater effect on the salt distribution in the aquifer than  
453 the water and salt exchange rates. As expected the USP was initially (pre-storm) larger for the  
454 simulations with lower fresh groundwater discharge (Figure 14a, Cases 8 and 9). As a  
455 counterbalance to the upper seawater recirculation, the increased fresh groundwater flux pushed  
456 back the wave-induced recirculation and thus the USP. Due to the reduced resistance to seawater  
457 recirculation, the USP expanded more in Cases 8 and 9 compared with Case 1 (Table 1, Figure  
458 14). For Case 9, the mass of salt in the USP was greatest at  $\sim 43$  d and the depth of the plume was  
459 greatest at  $\sim 61$  d. This was delayed compared to the cases with higher  $Q_f$  due to the deeper flow  
460 paths and slower transport (advective) of recirculating saltwater particles.

461 The time for the salt mass in the upper aquifer to return to within 10% (surplus) of the pre-storm  
462 conditions was 46 d for Case 7, 62 d for Case 1, 88 d for Case 8 and 92 d for Case 9. Again the  
463 longer recovery period for the cases with reduced  $Q_f$  was linked with deeper (and longer) flow  
464 paths of the recirculating seawater. Also, once entrained in the fresh groundwater streamlines the  
465 velocity of the discharging saltwater particles was less for simulations with lower  $Q_f$ . The transit  
466 times for the discharging freshwater particles increased for the cases with reduced  $Q_f$  and the  
467 flow paths of the shallow freshwater particles were more perturbed for Cases 8 and 9 compared  
468 with Cases 1 and 7. The transit times for saltwater particles recirculating through the system for  
469 the different cases are shown in Figure 15a. With the exception of Case 9 there was a strong  
470 correlation between the maximum transit times and the 10% recovery time. For Case 9, the

471 maximum advective transit time for recirculating saltwater particles was longer (108 d) than the  
472 10% recovery time (96 d). Despite this, at the end of the simulation (160 d) there was still 5.5%  
473 of surplus salt remaining in the aquifer relative to the pre-storm conditions. This suggests that the  
474 dispersive transport and associated fresh-saltwater mixing may become more important as the  
475 advective forcing in the aquifer (driven by the fresh groundwater flux) decreases.

### 476 **3.5 Effect of hydraulic conductivity**

477 The hydraulic conductivity ( $K$ ) of the aquifer significantly altered the storm-driven fluxes across  
478 the aquifer-ocean interface and the nearshore flow and salt transport. The total storm-induced  
479 seawater influx increased from  $12.2 \text{ m}^3\text{m}^{-1}$  to  $54.1 \text{ m}^3\text{m}^{-1}$  as  $K$  increased from  $6.67 \text{ md}^{-1}$  (Case  
480 12) to  $50 \text{ md}^{-1}$  (Case 10; Table 1). Consistent with the influx rates, the storm-induced change in  
481 the USP salt mass was much greater for the cases with higher  $K$  ( $282 \text{ kgm}^{-1}$  for Case 12 c.f.  $2412$   
482  $\text{kgm}^{-1}$  for Case 10, Figure 16a). The initial horizontal expansion of the USP was similar for all  
483 cases (as indicated by the USP  $x$ -centroid location) but higher  $K$  led to deeper wave-induced flow  
484 recirculation and thus deeper expansion of the USP (Figure 16b,c). For Case 10, the USP became  
485 sufficiently large that it merged with the saltwater wedge and pushed its interface seaward  
486 (Figure 17c,d). After the storm receded, the initial freshwater discharge zone re-formed as the  
487 freshwater streamlines returned to pre-storm conditions and forced the fresh groundwater to  
488 discharge near the shoreline (Figure 17d,e). The complex nearshore salt distribution for Case 10  
489 led to differences in the behavior of the USP plume centroid and mixing after 20 d compared to  
490 the cases with lower  $K$  (Figure 16). Although the storm-induced change in USP salt mass  
491 increased as  $K$  increased (Figure 16), the 10% recovery time decreased to 38 d when  $K = 50 \text{ md}^{-1}$   
492 (Case 10). This indicates that despite the larger disturbance, the salt distribution will return more  
493 rapidly to pre-storm conditions in coarse sand and gravel beach aquifers. The variances

494 calculated for the USP (Figure 16d,e) suggest that the salt-freshwater mixing induced by a wave  
495 event will be greater in a more permeable aquifer. It should be noted that although only isotropic  
496 conditions were examined, anisotropy ratios ( $K_x/K_z$ ) in beach aquifers up to 50 are not  
497 uncommon [Urish, 2004]. It is expected anisotropy (reduced  $K_z$ ) would decrease the depth of the  
498 wave-induced flow circulations and this would in turn limit the downward expansion of the  
499 upper saline plume over the wave event and subsequently the salt-freshwater mixing.

### 500 **3.6 Effect of beach slope ( $\beta$ )**

501 The beach slope controls the width of the wave set-up zone, and as a result, the width of the  
502 wave-induced recirculations and USP, in addition to the horizontal excursion of the shoreline  
503 over the wave event. Simulations performed for steep to mildly sloped beaches ( $\beta = 0.1$  in Case  
504 1,  $\beta = 0.075$  in Case 13 and  $\beta = 0.05$  in Case 14) show that the influence of  $\beta$  on the storm-  
505 induced exchange rates across the aquifer-ocean interface is non-monotonic. The instantaneous  
506 and total storm-driven water influx was highest for the case with intermediate beach slope (Case  
507 13, Table 1). As the beach steepens, the excursion of the shoreline over the wave event is  
508 reduced and therefore there is less area (potential) for seawater infiltration. In contrast, as the  
509 beach flattens, although the horizontal shoreline excursion over the wave event is greater, the  
510 onshore pressure gradient that drives infiltration is reduced and as a result there is less influx of  
511 seawater into the aquifer. However, the effect of  $\beta$  is small relative to the factors explored above:  
512 total storm-driven influx varied only from  $20.2 \text{ m}^3\text{m}^{-1}$  for Case 1,  $23.8 \text{ m}^3\text{m}^{-1}$  for Case 13 and  
513  $22.2 \text{ m}^3\text{m}^{-1}$  for Case 14. Consistent with the total water influxes, the change in USP salt mass due  
514 to the wave event was similar for all cases and slightly higher for Case 13 (Table 1, Figure 18a).  
515 Despite this, the time for the mass in the USP plume to return to within 10% (surplus) of the pre-  
516 storm conditions significantly increased as the beach flattened (131 d for Case 14, 86 d for Case

517 13 and 62 d for Case 1, Figure 18a). The increase in recovery time is caused by longer transport  
518 pathways and thus recirculating seawater transit times due to the greater shoreline excursion. In  
519 addition, the milder beach slope limits the beach's drainage capacity following the wave event.  
520 The larger shoreline excursion for Case 14 also led to the greatest horizontal shift (landward) in  
521 the centroid of the USP and greatest horizontal spreading of the plume (Figure 18b,d). The  
522 downwards expansion of the USP is reduced and more gradual for Case 14 due to the shallower  
523 and wider wave-induced recirculation (Figure 18c,e).

#### 524 **4. Conclusions**

525 Numerical simulations revealed that intensified wave conditions generated by an offshore storm  
526 significantly perturb the flow and salt transport in a subterranean estuary. The seawater influx to  
527 a near-shore aquifer was also shown to significantly increase during an intensified wave event.  
528 This may lead to large influxes of chemical species such as oxygen, organic matter and nutrients  
529 to a subterranean estuary. The increased availability of these chemicals combined with enhanced  
530 wave-induced salt-freshwater mixing may alter the geochemical conditions in a subterranean  
531 estuary including the stability of geochemical zonations. In turn this may affect the fate of  
532 chemicals discharging and recirculating through a near-shore aquifer. The water efflux also  
533 increased in response to the intensified wave conditions. While this increase was caused by  
534 higher seawater recirculation rates, it would modify temporal SGD patterns and hence loading  
535 rates of chemical species to the coastal sea.

536 Although wave events of larger magnitude (wave height) and/or longer duration cause greater  
537 disturbances to the near-shore salinity distribution and exchange fluxes, a small increase in wave  
538 height has the potential to affect processes in a subterranean estuary particularly for nearshore  
539 aquifers of higher permeability and with lower fresh groundwater flux. The simulations showed

540 that while exchange fluxes and groundwater flow patterns return to pre-storm conditions  
541 relatively quickly, it may take up to the order of months for the salinity distribution in a near-  
542 shore aquifer to recover. As small wave events occur frequently along coastlines, the next wave  
543 event may occur before the aquifer has recovered. This will result in a complex and dynamic salt  
544 distribution that is controlled by the combined frequency and magnitude of these events. The  
545 increase in wave height was shown to more significantly impact the near-shore aquifer dynamics  
546 and aquifer recovery time than the duration of the wave event. For shorter duration events,  
547 especially when the beach is flatter and the beach aquifer is less permeable, the depth of the  
548 storm-induced seawater recirculation and vertical expansion of the USP are limited to the  
549 shallow aquifer sediments.

550 Previous field investigations of near-shore aquifer dynamics and/or SGD often draw conclusions  
551 from single monitoring events. The long recovery times revealed here indicate that analyses need  
552 to consider the oceanic forcing conditions in the months leading up to a monitoring event. The  
553 results also highlight the need for long-term continuous monitoring at field sites. Only single  
554 synthetic wave events were considered here. Simulations considering real time-series of wave  
555 height over long continuous periods would provide further insight into the dynamic response of  
556 the aquifer to long-term varying wave conditions. Understanding the variability induced by  
557 changing wave conditions is needed to understand the complexity of the processes occurring in a  
558 subterranean estuary. This complexity will be further increased by non-planar beach slopes,  
559 aquifer heterogeneities, and the interplay with, for example, complex tidal forcing (including  
560 spring-neap signal) and seasonal fresh groundwater flux variations. These additional factors and  
561 processes should be examined in future investigations to further explore the complexity of the  
562 coastal groundwater system, as revealed in this study.

563 **Acknowledgements**

564 This research was supported by NSERC Discovery Grant (386448-2010). The authors would like  
565 to thank the three reviewers whose helpful comments improved the paper.

566 **References**

567 Abarca, E., H. Karam, H. F. Hemond, and C. F. Harvey (2013), Transient groundwater dynamics  
568 in a coastal aquifer: The effects of tides, the lunar cycle, and the beach profile, *Water Resour.*  
569 *Res.*, *49*, 2473–2488, doi:10.1002/wrcr.20075.

570 Anschutz, P., T. Smith, A. Mouret, J. Deborde, S. Bujan, D. Poirier, and P. Lecroart (2009),  
571 Tidal sands as biogeochemical reactors, *Estuar. Coast. Shelf Sci.*, *84*(1), 84–90,  
572 doi:10.1016/j.ecss.2009.06.015.

573 Appelo, C. A. J. (1994), Cation and proton exchange, pH variations, and carbonate reactions in a  
574 freshening aquifer, *Water Resour. Res.*, *30*(10), 2793-2805, doi: 10.1029/94WR01048.

575 Bakhtyar, R., D. A. Barry, and A. Brovelli (2012), Numerical experiments on interactions  
576 between wave motion and variable-density coastal aquifers, *Coast. Eng.*, *60*(1), 95-108, doi:  
577 10.1016/j.coastaleng.2011.09.001.

578 Bakhtyar, R., A. Brovelli, D. A. Barry, C. Robinson, and L. Li (2013), Transport of variable-  
579 density solute plumes in beach aquifers in response to oceanic forcing, *Adv. Water Resour.*, *53*,  
580 208-224, doi: 10.1016/j.advwatres.2012.11.009.

581 Boufadel, M. C. (2000), A mechanistic study of nonlinear solute transport in a groundwater-  
582 surface water system under steady state and transient hydraulic conditions, *Water Resour. Res.*,  
583 *36*(9), 2549-2565, doi: 10.1029/2000WR900159.

584 Brovelli, A., X. Mao, and D. A. Barry (2007), Numerical modeling of tidal influence on density-  
585 dependent contaminant transport, *Water Resour. Res.*, 43(10), W10426, doi:  
586 10.1029/2006WR005173.

587 Burnett, W. C., H. Bokuniewicz, M. Huettel, W. S. Moore, and M. Taniguchi (2003),  
588 Groundwater inputs to the coastal zone, *Biogeochemistry*, 66(1-2), 3-33, doi:  
589 10.1023/B: BIOG.0000006066.21240.53.

590 Carsel, R. F., and R. S. Parrish (1988), Developing joint probability distributions of soil water  
591 retention characteristics, *Water Resour. Res.*, 24(5), 755-769, doi:10.1029/WR024i005p00755.

592 Cartwright, N., L. Li, and P. Nielsen (2004), Response of salt-freshwater interface in a coastal  
593 aquifer to a wave-induced groundwater pulse: Field observations and modelling, *Adv. Water*  
594 *Resour.*, 27(3), 297-303, doi:10.1016/j.advwatres.2003.12.005.

595 Charette, M. A., E. R. Sholkovitz, and C. M. Hansel (2005), Trace element cycling in a  
596 subterranean estuary: Part 1. Geochemistry of the permeable sediments, *Geochem et Cosmochim*  
597 *Acta*, 69(8), 2095-2109, doi:10.1016/j.gca.2004.10.024.

598 Diersch, H. J., and O. Kolditz (2002), Variable-density flow and transport in porous media:  
599 approaches and challenges, *Adv. Water Resour.*, 25(8-12), 899-944, doi:10.1016/S0309-  
600 1708(02)00063-5.

601 Hays, R. L., and W. J. Ullman (2007), Dissolved nutrient fluxes through a sandy estuarine  
602 beachface (Cape Henlopen, Delaware, U.S.A.): Contributions from fresh groundwater discharge,  
603 seawater recycling, and diagenesis, *Estuar. Coasts*, 30(4), 710-724, doi: 10.1007/BF02841967.

604 Johannes, R. E. (1980), The ecological significance of the submarine discharge of groundwater,  
605 *Mar. Ecol. Prog. Ser.*, 3, 365-373.

606 Kroeger, K. D., and M. A. Charette (2008), Nitrogen biogeochemistry of submarine groundwater  
607 discharge, *Limnol. Oceanogr.*, 53(3), 1025-1039, doi: 10.4319/lo.2008.53.3.1025.

608 Kuan, W. K., G. Jin, P. Xin, C. Robinson, B. Gibbes, and L. Li (2012), Tidal influence on  
609 seawater intrusion in unconfined coastal aquifers, *Water Resour. Res.*, 48(2), W02502, doi:  
610 10.1029/2011WR010678.

611 Lenkopane, M., A. D. Werner, D. A. Lockington, and L. Li (2009), Influence of variable salinity  
612 conditions in a tidal creek on riparian groundwater flow and salinity dynamics, *J. Hydrol.*, 375(3-  
613 4), 536-545, doi:10.1016/j.jhydrol.2009.07.004.

614 Li, L., and D. A. Barry (2000), Wave-induced beach groundwater flow, *Adv. Water Resour.*,  
615 23(4), 325-337.

616 Li, L., D. A. Barry, C. B. Pattiaratchi, and G. Masselink (2002), BeachWin: modelling  
617 groundwater effects on swash sediment transport and beach profile changes, *Environ. Model.*  
618 *Softw.*, 17(3), 313-320, doi:10.1016/S1364-8152(01)00066-4.

619 Li, L., N. Cartwright, P. Nielsen, and D. Lockington (2004), Response of coastal groundwater  
620 table to offshore storms, *China Ocean Eng.*, 18(3), 423-431.

621 Longuet-Higgins, M. S. (1983), Wave set-up, percolation and undertow in the surf zone, *Proc.*  
622 *Royal Soc. Lond. A*, 390(1799), 283-291, doi:10.1098/rspa.1983.0132.

623 Loveless, A. M., and C. E. Oldham (2010), Natural attenuation of nitrogen in groundwater  
624 discharging through a sandy beach, *Biogeochemistry*, 98(1-3), 75-87, doi: 10.1007/s10533-009-  
625 9377-x.

626 Mango, A. J., M. W. Schmeckle, and D. J. Furbish (2004), Tidally induced groundwater  
627 circulation in an unconfined coastal aquifer modeled with a Hele-Shaw cell, *Geology*, 32(3),  
628 233-236, doi: 10.1130/G19922.1

629 Mao, X., P. Enot, D. A. Barry, L. Li, A. Binley, and D.-S. Jeng (2006), Tidal influence on  
630 behaviour of a coastal aquifer adjacent to a low-relief estuary, *J. Hydrol.*, 327(1-2), 110-127,  
631 doi:10.1016/j.jhydrol.2005.11.030.

632 Masselink, G., and A. D. Short (1993), The effect of tide range on beach morphodynamics and  
633 morphology: A conceptual beach model, *J Coastal Res*, 9(3), 785-800.

634 Moore, W. S. (1999), The subterranean estuary: A reaction zone of ground water and sea water,  
635 *Mar. Chem.*, 65(1-2), 111-125, doi:10.1016/S0304-4203(99)00014-6.

636 Nielson, P. (2009), *Coastal and Estuarine Processes, Advanced Series on Ocean Engineering*,  
637 *Vol. 29*, , World Scientific, Singapore.

638 Robinson, C., B. Gibbes, and L. Li (2006), Driving mechanisms for flow and salt transport in a  
639 subterranean estuary, *Geophys. Res. Lett.*, 33(3), L03402, doi:10.1029/2005GL025247.

640 Robinson, C., B. Gibbes, H. Carey, and L. Li (2007a), Salt-freshwater dynamics in a  
641 subterranean estuary over a spring-neap tidal cycle, *J. Geophys. Res.*, 112(C9), C09007,  
642 doi:10.1029/2006JC003888.

643 Robinson, C., L. Li, and D. A. Barry (2007b), Effect of tidal forcing on a subterranean estuary,  
644 *Adv. Water Resour.*, 30(4), 851-865, doi:10.1016/j.advwatres.2006.07.006.

645 Robinson, C., A. Brovelli, D. A. Barry, and L. Li (2009), Tidal influence on BTEX  
646 biodegradation in sandy coastal aquifers, *Adv. Water Resour.*, 32(1), 16–28,  
647 doi:10.1016/j.advwatres.2008.09.008.

648 Shand, T. D., I. D. Goodwin, M. A. Mole, J. T. Carley, S. Browning, I. G. Coghlan, M. D.  
649 Harley, W. L. Peirson, Z. J. You, and M. A. Kulmar (2010), NSW Coastal storms and extreme  
650 waves, paper presented at 19th NSW Coastal Conference, Batemans Bay, NSW.

651 Slomp, C. P., and P. van Cappellen (2004), Nutrient inputs to the coastal ocean through  
652 submarine groundwater discharge: controls and potential impact, *J. Hydrol.*, 295(1-4), 64-86,  
653 doi:10.1016/j.jhydrol.2004.02.018.

654 Smith, A. J. (2004), Mixed convection and density-dependent seawater circulation in coastal  
655 aquifers, *Water Resour. Res.*, 40(8), W08309, doi:10.1029/2003WR002977.

656 Spiteri, C., P. Regnier, C. P. Slomp, and M. A. Charette (2005), pH-dependent iron oxide  
657 precipitation in a subterranean estuary, *J. Geochem. Explor.*, 88(1-3), 399-403,  
658 doi:10.1016/j.gexplo.2005.08.084.

659 Spiteri, C., C. Slomp, K. Tuncay, and C. Meile (2008a), Modeling biogeochemical processes in  
660 subterranean estuaries: Effect of flow dynamics and redox conditions on submarine groundwater  
661 discharge of nutrients, *Water Resour. Res.*, 44(2), W04701, doi: 10.1029/2007WR006071.

662 Spiteri, C., C. P. Slomp, M. A. Charette, K. Tuncay, and C. Meile (2008b), Flow and nutrient  
663 dynamics in a subterranean estuary (Waquoit Bay, MA, USA): Field data and reactive transport  
664 modeling, *Geochem. Cosmochim. Acta*, 72(14), 3398-3412, 10.1016/j.gca.2008.04.027.

665 Urish, D. W. (2004), Determination of the temporal and spatial distribution of beach face  
666 seepage, in *Coastal aquifer management: monitoring, modelling and case studies*, edited by A.  
667 H. D. Cheng and D. Ouzar, pp. 143-165, Lewis Publishers, New York.

668 van Genuchten, M. T. (1980), A closed form equation for predicting the hydraulic conductivity  
669 of unsaturated soils, *Soil Sci. Soc. Am. J.*, 44(5), 892-898,  
670 doi:10.2136/sssaj1980.03615995004400050002x.

671 Voss, C., and W. Souza (1987), Variable density flow and solute transport simulation of regional  
672 aquifers containing a narrow freshwater-saltwater transition zone, *Water Resour. Res.*, 23(10),  
673 1851-1866, doi:10.1029/WR023i010p01851.

674 Voss, C. I., and A. M. Provost (2002), A model for saturated-unsaturated variable-density  
675 groundwater flow with solute or energy transport, Water Res. Invest. Rep., 02-4231,, U.S. Geol.  
676 Surv., Reston, Va.

677 Werner, A. D., M. Bakker, V. E. A. Post, A. Vandenbohede, C. Lu, B. Ataie-Ashtiani, C. T.  
678 Simmons, and D. A. Barry (2013), Seawater intrusion processes, investigation and management:  
679 Recent advances and future challenges, *Adv. Water Resour.*, 51, 3-26, doi:  
680 10.1016/j.advwatres.2012.03.004.

681 Westbrook, S. J., J. L. Rayner, G. B. Davis, T. P. Clement, P. L. Bjerg, and S. J. Fisher (2005),  
682 Interaction between shallow groundwater, saline surface water and contaminant discharge at a  
683 seasonally and tidally forced estuarine boundary, *J. Hydrol.*, 302(1-4), 255-269,  
684 doi:10.1016/j.jhydrol.2004.07.007.

685 Xin, P., C. Robinson, L. Li, D. A. Barry, and R. Bakhtyar (2010), Effects of wave forcing on a  
686 subterranean estuary, *Water Resour. Res.*, 46(12), W12505, doi:10.1029/2010WR009632.

687

688 Table 1. Simulated cases with model parameter values and key results.

Case	Input Parameters					Salt mass in USP				Water Influx/Efflux		
	$H_{rms}^{INC}$ (m)	$F$ (d)	$Q_f$ ( $m^3d^{-1}$ )	$K$ ( $md^{-1}$ )	$\beta$ (-)	Change in salt mass ( $kgm^{-1}$ )	Maximum salt mass ( $kgm^{-1}$ )	5% recovery time (d)	10% recovery time (d)	Total storm- driven influx ( $m^3d^{-1}m^{-1}$ )	Maximum influx ( $m^3d^{-1}m^{-1}$ )	Maximum efflux ( $m^3d^{-1}m^{-1}$ )
1	3	2	2.1	10	0.1	369	471	79	62	20.2	7.6	5.8
2	5	2	2.1	10	0.1	623	726	134	99	33.9	13.3	7.5
3	6	2	2.1	10	0.1	758	861	-	115	53.8	17.3	8.2
4	2	2	2.1	10	0.1	241	344	59	49	16.6	5.8	5.0
5	3	1	2.1	10	0.1	216	319	-	154	11.1	8.7	5.5
6	3	0.5	2.1	10	0.1	127	230	-	78	6.0	10.5	5.2
7	3	2	3.15	10	0.1	325	375	55	46	18.1	7.3	6.4
8	3	2	1.4	10	0.1	430	613	124	88	22.3	8.2	5.5
9	3	2	1	10	0.1	477	752	-	96	23.2	8.3	5.2
10	3	2	2.1	50	0.1	2412	3101	52	48	54.1	37.7	30.4
11	3	2	2.1	21	0.1	749	1030	63	51	39.7	16.7	12.1
12	3	2	2.1	6.66	0.1	282	233	83	70	12.2	5.7	4.1
13	3	2	2.1	10	0.075	379	486	104	86	23.8	8.1	5.4
14	3	2	2.1	10	0.05	351	449	-	126	22.2	7.8	4.6

690 **Figure Captions**

691 Figure 1. (a) Conceptual diagram of the water levels, groundwater flows and salinity distribution  
692 in a near-shore aquifer exposed to waves. The still water level (SWL), instantaneous water  
693 surface (thick solid line) and wave set-up profiles (phase-averaged water surface) for the steady  
694 state condition (pre- and post-storm, dashed line) and storm peak (dash-dotted line) are shown.  
695 The upper saline plume (USP) formed by wave-driven recirculation (WDR) is shown in addition  
696 to the potential expansion of the USP in response to the storm. The saltwater wedge formed by  
697 density-driven recirculation (DDR) is also shown. (b) Numerical model domain and parameters.  
698 The dashed box in (b) illustrates the near-shore zone highlighted in (a).

699 Figure 2. Synthetic wave events simulated. Cases 7-14 consider the same wave event as Case 1.

700 Figure 3. Instantaneous salt concentration (color bars are salinity in ppt) and flow velocities  
701 (vectors) for Case 1. The elapsed times are given in the figure legends. The black lines indicate  
702 the wave set-up and watertable elevation. The results for days 62 and 106 are provided as these  
703 correspond to the times when the mass of salt in the upper aquifer domain had recovered to  
704 within 10% and 1% (surplus), respectively, of the pre-storm condition.

705 Figure 4. (a) Total salt mass per unit width of aquifer in the USP, (b)  $x$ -coordinate of centroid  
706 ( $x_c$ ) and (c)  $z$ -coordinate of centroid ( $z_c$ ) of salt in the USP for Case 1 ( $H_{rms}^{INC} = 3$  m), Case 2 ( $H_{rms}^{INC}$   
707 = 5 m), Case 3 ( $H_{rms}^{INC} = 6$  m) and Case 4 ( $H_{rms}^{INC} = 2$  m). The time of the storm peak (6 d) is  
708 indicated by the vertical black dashed line.

709 Figure 5. Simulated flow paths for saltwater particles and freshwater particles transported  
710 through the near-shore aquifer for (a) Case 1 and (b) steady state conditions with  $H_{rms} = 1$  m.  
711 Transit times along each flow path are depicted by the colored line shading. Note that in (a) the

712 freshwater and saltwater particle flow lines cross in space but not in time. Under the steady-state  
713 condition, there was only a narrow wave-induced seawater infiltration zone from  $x = -5$  to  $-2.5$  m  
714 and infiltrating saltwater particles had considerably shorter transit times. The blue-dashed line  
715 above the sediment-water interface (black-solid line) in (a) depicts the mean water level at the  
716 peak of the wave event ( $H_{rms} = 4$  m) and the blue-solid line in (a) and (b) depicts the steady state  
717 mean water level ( $H_{rms} = 1$ ).

718 Figure 6. Transit times for seawater particles to recirculate through the aquifer, varying with the  
719 infiltration  $x$ -location along the aquifer-ocean interface for cases with varying (a) magnitude of  
720 the wave event ( $H_{rms}^{INC}$ ) and (b) wave event duration ( $F$ ). The horizontal lines denote the time  
721 calculated for the mass of salt in the USP to recover to within 10% (dashed line), 5% (dotted  
722 line) and 1% (dash-dotted line) of the pre-storm condition. The recovery times for Cases 2, 3 and  
723 4 are shown in (a) and recovery times for Case 1 (red lines) are shown in (b). The recovery times  
724 are not shown for Cases 5 and 6 as they are similar to that of Case 1. For Case 2 the mass in the  
725 USP does not return to within 1% and for Case 3 it does not return to within 5% of the pre-storm  
726 conditions over the 160 d simulation period.

727 Figure 7. (a) Horizontal variance ( $\sigma_{xx}$ ), and (b) vertical variance ( $\sigma_{zz}$ ) of salt in the USP for Case  
728 1 ( $H_{rms}^{INC} = 3$  m), Case 2 ( $H_{rms}^{INC} = 5$  m), Case 3 ( $H_{rms}^{INC} = 6$  m) and Case 4 ( $H_{rms}^{INC} = 2$  m). The particle  
729 tracking results at 6 d (maximum  $\sigma_{xx}$ ) and 40 d (maximum  $\sigma_{zz}$ ) for Case 1 are provided in (c) and  
730 (d), respectively. The black lines show the flow paths for saltwater particles originating along the  
731 aquifer-ocean interface and the grey lines show the flow paths for freshwater particles  
732 originating at  $x = -15$  m. The similar locations of the freshwater and saltwater particles indicate  
733 mixing of the two waters.

734 Figure 8. (a) Total salt mass per unit width of aquifer in the saltwater wedge, and (b)  $x$ -  
735 coordinate of centroid ( $x_c$ ), (c)  $z$ -coordinate of centroid ( $z_c$ ) of the saltwater wedge for Case 1  
736 ( $H_{rms}^{INC} = 3$  m), Case 2 ( $H_{rms}^{INC} = 5$  m), Case 3 ( $H_{rms}^{INC} = 6$  m) and Case 4 ( $H_{rms}^{INC} = 2$  m). The time of the  
737 peak of the (6 d) is indicated by the vertical black dashed line.

738 Figure 9. (a) Water influx, (b) water efflux, (c) salt influx and (d) salt efflux across the aquifer-  
739 ocean interface for Case 1 ( $H_{rms}^{INC} = 3$  m), Case 2 ( $H_{rms}^{INC} = 5$  m), Case 3 ( $H_{rms}^{INC} = 6$  m) and Case 4  
740 ( $H_{rms}^{INC} = 2$  m). The time of the storm peak (6 d) is indicated by the vertical black dashed line.

741 Figure 10. Instantaneous salt concentration (color bars are salinity in ppt) and flow velocities  
742 (vectors) for Case 2. The elapsed times are given in the figure legends. The black lines indicate  
743 the wave set-up and watertable elevation. The result for day 102.5 corresponds to the time when  
744 the mass of salt in the upper aquifer had recovered to within 10% (surplus) of the pre-storm  
745 condition. At the end of the simulation (160 d) the mass of salt in the upper aquifer had  
746 recovered to within 2.5% (surplus) of the pre-storm condition.

747 Figure 11. (a) Water influx and (b) water efflux for Case 1 ( $F = 2$ ), Case 5 ( $F = 1$ ) and Case 6 ( $F$   
748  $= 0.5$ ). The time of the storm peak (6 d) is indicated by the vertical black dashed line.

749 Figure 12. (a) Total salt mass per unit width of aquifer in USP and (b)  $x$ -coordinate of centroid  
750 ( $x_c$ ), (c)  $z$ -coordinate of centroid ( $z_c$ ), (d) horizontal variance ( $\sigma_{xx}$ ), and (e) vertical variance ( $\sigma_{zz}$ )  
751 of salt in the USP for Case 1 ( $F = 2$ ), Case 5 ( $F = 1$ ) and Case 6 ( $F = 0.5$ ). The time of the storm  
752 peak (6 d) is indicated by the vertical black dashed line.

753 Figure 13. (a) Water influx and (b) water efflux for Case 1 ( $Q_f = 2.1$  m<sup>3</sup>d<sup>-1</sup>), Case 7 ( $Q_f = 3.15$   
754 m<sup>3</sup>d<sup>-1</sup>) and Case 8 ( $Q_f = 1.4$  m<sup>3</sup>d<sup>-1</sup>) and Case 9 ( $Q_f = 1$  m<sup>3</sup>d<sup>-1</sup>). The time of the storm peak (6 d) is  
755 indicated by the vertical black line.

756 Figure 14. (a) Total salt mass per unit width of aquifer in USP and (b)  $x$ -coordinate of centroid  
757 ( $x_c$ ), (c)  $z$ -coordinate of centroid ( $z_c$ ), (d) horizontal variance ( $\sigma_{xx}$ ), and (e) vertical variance ( $\sigma_{zz}$ )  
758 of salt in the USP for Case 1 ( $Q_f = 2.1 \text{ m}^3\text{d}^{-1}$ ), Case 7 ( $Q_f = 3.15 \text{ m}^3\text{d}^{-1}$ ), Case 8 ( $Q_f = 1.4 \text{ m}^3\text{d}^{-1}$ )  
759 and Case 9 ( $Q_f = 1 \text{ m}^3\text{d}^{-1}$ ). The time of the storm peak (6 d) is indicated by the vertical black  
760 dashed line.

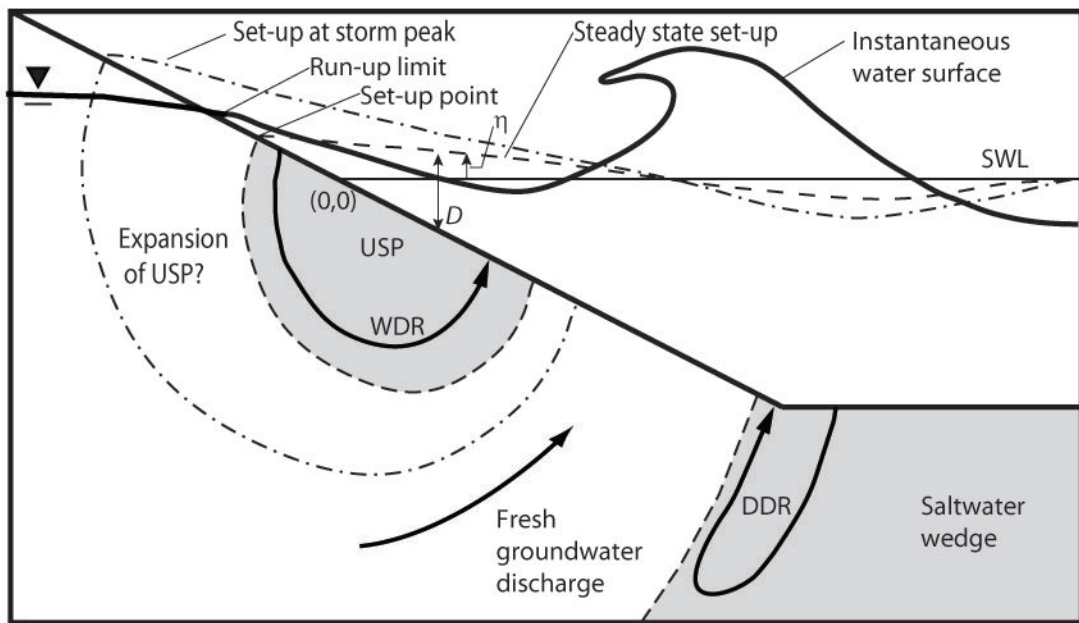
761 Figure 15. Transit times for seawater particles to recirculate through the aquifer, varying with the  
762 infiltration  $x$ -location along the aquifer-ocean interface for simulations with varying  $Q_f$  (Cases 1  
763 and 7-9). The horizontal lines denote the time calculated for the mass of salt in the USP to  
764 recover to within 10% (dashed line) of the pre-storm conditions for each case.

765 Figure 16. (a) Total salt mass per unit width of aquifer in USP and (b)  $x$ -coordinate of centroid  
766 ( $x_c$ ), (c)  $z$ -coordinate of centroid ( $z_c$ ), (d) horizontal variance ( $\sigma_{xx}$ ), and (e) vertical variance ( $\sigma_{zz}$ )  
767 of salt in the USP for Case 1 ( $K = 10 \text{ md}^{-1}$ ), Case 10 ( $K = 50 \text{ md}^{-1}$ ), Case 11 ( $K = 21 \text{ md}^{-1}$ ) and  
768 Case 12 ( $K = 6.7 \text{ md}^{-1}$ ). The time of the storm peak (6 d) is indicated by the vertical black dashed  
769 line.

770 Figure 17. Instantaneous salt concentration (color bars are salinity in ppt) and flow velocities  
771 (vectors) for Case 10 ( $K = 50 \text{ m/d}$ ). The elapsed times are given in the figure legends. The black  
772 lines indicate the wave set-up and watertable elevation.

773 Figure 18. (a) Total salt mass per unit width of aquifer in USP and (b)  $x$ -coordinate of centroid  
774 ( $x_c$ ), (c)  $z$ -coordinate of centroid ( $z_c$ ), (d) horizontal variance ( $\sigma_{xx}$ ), and (e) vertical variance ( $\sigma_{zz}$ )  
775 of salt in the USP for Case 1 ( $\beta = 0.1$ ), Case 13 ( $\beta = 0.075$ ) and Case 14 ( $\beta = 0.05$ ). The time of  
776 the storm peak (6 d) is indicated by the vertical black dashed line.

(a)



(b)

